applied sciences

MDPI

Article

Structural and Magnetic Properties of Nanosized Half-Doped Rare-Earth $Ho_{0.5}Ca_{0.5}MnO_3$ Manganite

Alessandra Geddo Lehmann [1,*], Giuseppe Muscas [1], Maurizio Ferretti [2], Emanuela Pusceddu [3], Davide Peddis [2,4] and Francesco Congiu [1,*]

[1] Dipartimento di Fisica, Università di Cagliari, S.P. Monserrato-Sestu km 0.700, 09042 Monserrato, Cagliari, Italy; giuseppe.muscas@dsf.unica.it
[2] Dipartimento di Chimica e Chimica Industriale, Università di Genova, Via Dodecaneso 31, 16146 Genova, Italy; ferretti@chimica.unige.it (M.F.); davide.peddis@unige.it (D.P.)
[3] Istituto di Biometereologia, CNR-IBIMET, Via G. Caproni 8, 50145 Firenze, Italy; emanuela.pusceddu@gmail.com
[4] Istituto di Struttura della Materia, CNR, Monterotondo Scalo, 00015 Roma, Italy
* Correspondence: alessandra.lehmann@dsf.unica.it (A.G.L.); franco.congiu@dsf.unica.it (F.C.)

Abstract: We investigated the structural and magnetic properties of 20 nm-sized nanoparticles of the half-doped manganite $Ho_{0.5}Ca_{0.5}MnO_3$ prepared by sol-gel approach. Neutron powder diffraction patterns show *Pbnm* orthorhombic symmetry for 10 K < T < 290 K, with lattice parameters a, b, and c in the relationship $c/\sqrt{2} < a < b$, indicating a cooperative Jahn–Teller effect, i.e., orbital ordering OO, from below room temperature. In contrast with the bulk samples, in the interval 250 < T < 300 K, the fingerprint of charge ordering (CO) does not manifest itself in the temperature dependence of lattice parameters. However, there are signs of CO in the temperature dependence of magnetization. Accordingly, below 100 K superlattice magnetic Bragg reflections arise, which are consistent with an antiferromagnetic phase strictly related to the bulk Mn ordering of a charge exchange-type (CE-type), but characterized by an increased fraction of ferromagnetic couplings between manganese species themselves. Our results show that in this narrow band half-doped manganite, size reduction only modifies the balance between the Anderson superexchange and Zener double exchange interactions, without destabilizing an overall very robust antiferromagnetic state.

Keywords: nanocrystalline half-doped manganites; charge ordering; SQUID magnetometry; neutron diffraction

Citation: Geddo Lehmann, A.; Muscas, G.; Ferretti, M.; Pusceddu, E.; Peddis, D.; Congiu, F. Structural and Magnetic Properties of Nanosized Half-Doped Rare-Earth $Ho_{0.5}Ca_{0.5}MnO_3$ Manganite. *Appl. Sci.* **2022**, *12*, 695. https://doi.org/10.3390/app12020695

Academic Editor: Manh-Huong Phan

Received: 6 December 2021
Accepted: 7 January 2022
Published: 11 January 2022

1. Introduction

Hole-doped colossal magnetoresistive (CMR) manganites with general formula $RE_{1-x}AE_xMnO_3$ (RE = trivalent rare-earth or La^{3+}, AE = divalent alkaline-earth metal Ca^{2+}, Sr^{2+}, Ba^{2+}, $0 \leq x \leq 1$, have been the subject of intense research for over twenty years thanks to their rich physics. This emerges from an outstanding variety of interconnected structural, electronic, and magnetic phase transitions, which lead to competing ground states, either metallic ferromagnetic (FM), with predominant Zener double exchange interaction [1], or insulating antiferromagnetic (AFM), with predominant Anderson superexchange interaction [2].

The crystal structures of the undoped phases depend on the RE size, changing from orthorhombic $GdFeO_3$-type perovskite (space group n. 62 *Pbnm*) for large rare-earths (from La to Tb), to hexagonal non-perovskite $LuMnO_3$-type (space group n. 185 $P6_3cm$) for small ones (from Dy to Lu, and Y). The partial substitution of RE^{3+} by a larger AE^{2+} ion induces an increase of the tolerance factor $t = [\langle r_A \rangle + r_O] / \left[\sqrt{2}(r_B + r_O) \right]$ expressed, with reference to the ABO_3 simple perovskite chemical formula, in terms of octahedral B-site cation and oxygen radii, respectively, r_B and r_O, and of the $<r_A>$ radius of the A-type cation, this latter

averaged between the two heterovalent A-type cations. As a consequence, the hexagonal structure is converted back to orthorhombic as long as the hole concentration exceeds a critical value x_c. In particular, all of the Ca-substituted half-doped phases $RE_{0.5}Ca_{0.5}MnO_3$ are distorted *Pbnm* perovskites.

The holmium-based system $Ho_{1-x}Ca_xMnO_3$ has some interesting peculiarities. $HoMnO_3$ belongs to the subgroup of $REMnO_3$ phases, which adopt the hexagonal $P6_3mc$ structure. $HoMnO_3$ is a multiferroic crystal in which ferroelectricity, with Curie temperature T_C as high as 875 K, is coupled to a frustrated AFM order with Néel temperature T_N of 72 K [3]. Since the size of Ho^{3+} is located just at the hexagonal and orthorhombic structural phase boundary, $HoMnO_3$ also exists as a metastable *Pbnm* perovskite [4,5], which retains ferroelectric properties, however, induced by the AFM ordering of the Mn ions occurring at T_N about 40 K, with a much lower ferroelectric Curie point of 30 K. On hole doping, $Ho_{1-x}Ca_xMnO_3$ suddenly converts to the stable *Pbnm* structure already at x = 0.1 [6]. Ferroelectricity still exists below T_N at x = 0.2 [6].

Half-doped $Ho_{0.5}Ca_{0.5}MnO_3$ presents a highly stable insulating AFM ground state. Ferroelectricity and its interconnections with antiferromagnetism have not been investigated anymore, outclassed in interest by the two phenomena of orbital ordering (OO) and charge ordering (CO), common to all Ca^{2+} half-doped $RE_{1-x}Ca_xMnO_3$ manganites. OO and CO are two of the most fascinating transitions, structural and electronic, exhibited by CMR manganites. An introduction to the subject can be found in [7]. OO derives from the presence of Jahn–Teller (JT) active Mn^{3+} ($t_{2g}{}^3e_g{}^1$) ions at the B octahedral site of the ABO_3 perovskite, the simple cubic cell of which is shown in Figure 1a, evidencing the vertex-by-vertex octahedra interconnections. OO consists in a cooperative distortion of the whole crystal structure at a critical temperature T_{OO}, which reflects the occurrence of a static long-range ordered pattern of the 3d e_g $x^2 - y^2$ or $3r^2 - z^2$ orbitals. Different OO patterns at different doping levels are associated with typical AFM structures, the most common of which, displayed in Figure 1b–d, are known as G-type (no OO at all), A-type (JT compressed octahedra), and C-type (JT elongated octahedra) [8].

CO superimposed to OO characterizes instead the half-doped (x = 0.5) or nearly half-doped compositions that contain nearly equal amounts of Jahn–Teller active Mn^{3+} and not-active Mn^{4+} ($t_{2g}{}^3e_g{}^0$) ions. In its most common description, CO is a real space 1:1 ordering of charge disproportionate $Mn^{(3+\delta)+}$ and $Mn^{(4-\delta)+}$ species, in which δ can be different from zero [7,8]. Such localization transition of the Mn^{3+} e_g electrons has been proposed to coincide with the establishment of a charge density wave (CDW), with amplitude determined by δ (with δ = 0 corresponding to the maximum amplitude) and allowed to be commensurate or incommensurate with the crystal lattice [9–11]. The CO transition is also a structural phase transformation with martensitic character: it is in fact a first-order orthorhombic to monoclinic ferroelastic transition at which CO twin domains nucleate and grow within the charge disordered (CD) matrix [12]. Very interestingly, especially for the analogy with a sliding CDW, the insulating AFM state with CO can be converted to electrically conductive FM by various means, which include the application of a magnetic field [13], electric field [14], or pressure [15]. The melting of the electronically localized CO state under the effect of an external magnetic field is indeed the phenomenon of colossal magnetoresistance itself.

The coexistence of OO and CO in half-doped manganites produces a complex AFM phase called the CE-type (acronymous of charge exchange-type). In such a structure (Figure 1e), Jahn–Teller distorted and undistorted octahedra alternate, leading to a checkerboard ordering of Mn^{3+} and Mn^{4+} in the (x,y) Cartesian planes, with planar zig-zag chains of ferromagnetically interacting Mn^{3+}-O-Mn^{4+} ions, with interchain AFM coupling (Figure 1e). The CE-type AFM structure is obtained by the stacking along the *z*-axis of such planes, with AFM interplanar coupling.

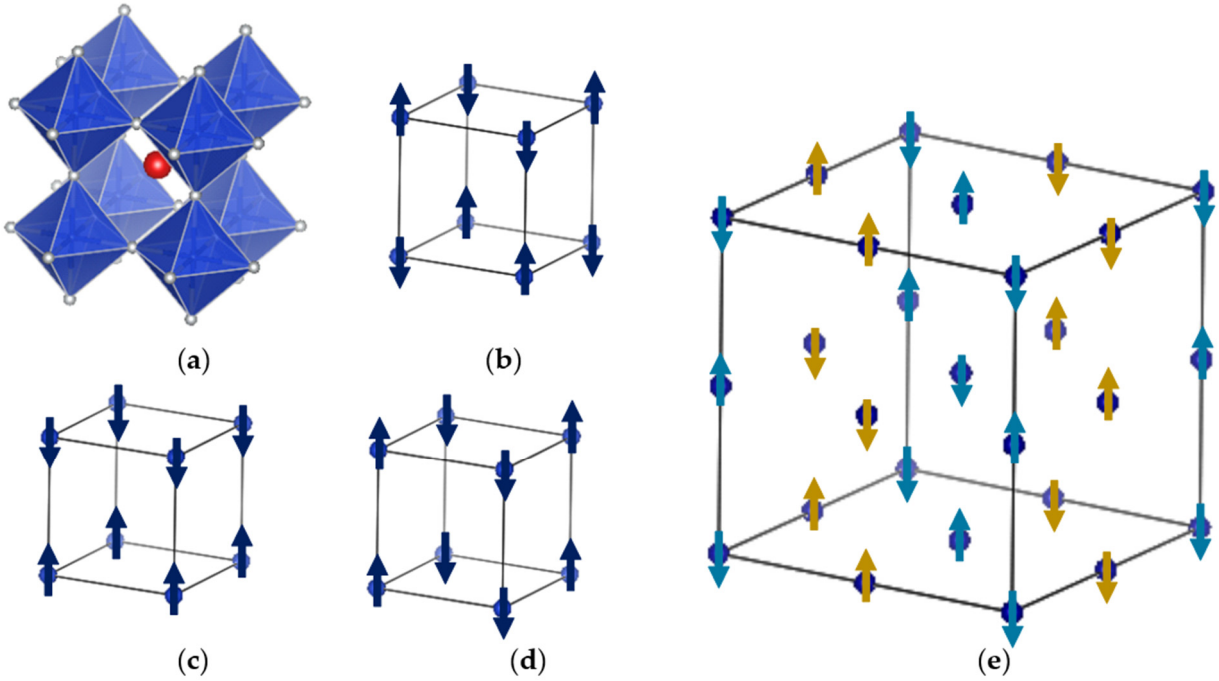

Figure 1. Sketch of the AFM structures encountered in hole-doped CMR manganites at different doping levels. (**a**) Representation of a simple perovskite $REMnO_3$, in which each Mn cation (at the center of octahedra) interacts magnetically with six first neighbors through oxygen atoms (small gray balls); the RE cation (red ball) is at the center of the unit cell. (**b**,**d**) Most common AFM structures (only the Mn species are represented, with magnetic moments shown as arrows pointing up and down): (**b**) G-type structure, typical of x = 1 compositions with only not Jahn–Teller active Mn^{4+} ions, in which all six first neighbors are antiferromagnetically coupled through Anderson superexchange interactions. (**c**) A-type and (**d**) C-type AFM structures, with, respectively, four over six and two over six ferromagnetic interactions, found when all (or the great majority) of Mn species are instead Jahn–Teller active Mn^{3+}. (**e**) CE-type charge and orbitally ordered AFM phase typical of half-doped compositions. Mn^{3+} and Mn^{4+} magnetic moments are represented by arrows of different colors (Mn^{4+} blue arrows, Mn^{3+} yellow arrows).

In the case of $Ho_{0.5}Ca_{0.5}MnO_3$, orbital ordering is present already at room temperature in bulk samples, while charge ordering takes place at T_{CO} = 270 K, even if in most samples there is no special feature in the temperature dependence of magnetization M(T) [16,17]. Antiferromagnetic correlations between Mn species develop at about 140 K, followed by a transition to a canted AFM phase with T_N of about 105 K. The AFM supercell, refined from neutron diffraction data, is compatible with a CE-type structure, with the aforementioned checkerboard pattern of two not equivalent Mn ions in the (a,b) plane of the paramagnetic *Pbnm* phase. A further magnetic transition is found at 40 K, interpreted as the passage to a glassy state [16] for the marked thermomagnetic irreversibility between the zero field cooled (ZFC) and field cooled (FC) magnetization M(T), similar to what was proposed for $Tb_{0.5}Ca_{0.5}MnO_3$ [18]. In the bulk, a fraction estimated of about 8% of the entire sample remains untransformed charge disordered (CD) and it is responsible for a ferromagnetic neutron Bragg scattering superimposed to the AFM one [16].

Later on, it has been shown that the destabilization of the CO CE-type AFM state of half-doped manganites, in favor of Zener ferromagnetism and conductive state, can also be achieved in polycrystalline samples through particle size reduction [19,20]. Different explanations have been reported for this size effect, among which the fundamental fact that, in nanoparticles, it may become difficult for the CD matrix to accommodate the long-range strain field associated with the transformed CO regions [21]. A second argument is based on the known characteristic of antiferromagnetic nanoparticles of having uncompensated

surface spins, not sharing the core magnetic ordering, the importance of which is the greater the higher the surface to volume ratio [22–25]. Moreover, the increase of unit cell volume with a decreasing particle size was proposed to affect the Mn e_g bandwidth, responsible for a changed balance between FM and AFM interactions [26]

In this work, we studied how the structural and magnetic properties are modified by particle size reduction in the particular case of $Ho_{0.5}Ca_{0.5}MnO_3$. Herewith, we shall consider the case of a very small particle size of about 20 nm.

2. Materials and Methods

$Ho_{0.5}Ca_{0.5}MnO_3$ nanoparticles were obtained by the Pechini method [27]. In this sol–gel process, stoichiometric amounts of precursors salts ($Ca(NO_3)_2$*$4H_2O$ (99.98%) Alfa Aesar, $Ho(NO_3)_3$*$5H_2O$ (99.99%) Alfa Aesar, $Mn(NO_3)_2$*$4H_2O$ (99.999%) Alfa Aesar) were dissolved in deionized water and mixed with ethylene glycol and citric acid, forming a stable solution. This solution was then heated on a thermal plate under constant stirring at 350 °C (625 K) to eliminate the excess of water and to accelerate the esterification reaction. After four hours, the solution underwent a drastic volume reduction, due to the formation of the gel. The gel was then calcinated at 400 °C (673 K) for 4 h. The result was a dark amorphous material, with light and crumbly consistency. The product pieces were crushed in a marble mortar until a fine powder was obtained. Finally, the material was allowed to re-crystallize by thermal treatment at a maximum temperature of 700 °C (973 K) for 7 h. X-ray fluorescence analysis provided for the Ho:Ca ratio the value of 49:51, in very good agreement with the nominal one. A bulk polycrystalline sample, the synthesis and characterization of which can be found in [16,28], was used as a reference for the magnetization measurements.

Neutron powder diffraction patterns were collected for 10 K < T < 300 K at the Institut Laue Langevin (ILL) in Grenoble (France) on the D20 diffractometer, a fixed-wavelength 2-axis instrument that can provide different combinations of resolution and intensity of incident neutron flux, obtained by the use of different monochromators and their take-off angles. Knowing which parts of the diffraction pattern contain the information for which the experiment is carried out in the first place permits the most convenient choice. Since the main aim of our experiment was to detect low-intensity magnetic Bragg reflections, which occur at low scattering angles, and given the expected broad Bragg peaks of the nanoparticles, the instrument was used in the low-resolution, high-intensity mode. The wavelength was set at 2.41 Å. Powdered samples were held in cylindrical vanadium containers with a nominal zero coherent scattering cross-section. Data were corrected for instrumental background and container scattering. The nuclear structure at different temperatures was refined according to the Rietveld method using FullProf software [29]; refinements were carried out using a file describing the instrumental resolution function, which is requested by FullProf to determine the average particle size. A discussion of the instrumental resolution function of neutron powder diffractometer can be found in [30], and specifically for D20 in [31].

An analysis of the size distribution of the manganite nanoparticle was also carried out by means of a transmission electron microscope (TEM) JEOL JEM 2010 operated at 200 kV and compared to the diffractometric result.

DC and AC magnetization measurements were performed using a Quantum Design MPMS XL5 Superconducting Quantum Interference Device (SQUID) magnetometer, equipped with a superconducting magnet generating fields up to 50 kOe and calibrated using a Pd standard. The sensitivity for the magnetic moment is 10^{-8} emu. The magnetometer is equipped with a system for setting to zero the applied field; the residual field during the zero field cooling is less than 10^{-2} Oe. The dependence of DC magnetization on temperature was studied by zero field cooling (ZFC) and field cooling (FC) measurements in the interval 5 K < T < 300 K. For measuring the temperature dependence of the ZFC magnetization (M_{ZFC}), the sample was cooled from 300 to 5 K in zero field, then the magnetic field was applied at 5 K and the magnetization was recorded on heating the sample. The

FC magnetization (M_{FC}) curves were recorded on cooling, keeping the sample in the same applied field. AC magnetization measurements were performed during warming, after zero field cooling, using an AC field with amplitude H_{AC} = 3.5 Oe at 10, 100, and 1000 Hz frequencies, under zero DC bias field.

3. Results and Discussion

Figure 2a shows a high-resolution transmission electron microscopy image of the nanoparticles. Despite accurate sonication, agglomeration of nanoparticles occurred, indicating high dipolar forces. The sample is constituted of ellipsoidal particles, mostly with a spherical shape. About 200 particles from several microscopy images were analyzed, and the average diameter was calculated measuring the minimal and maximal diameters for each one. A lognormal distribution was used to fit the diameter distribution resulting in the average diameter of 21.2(3) nm with a standard deviation of 3 nm and a coefficient of variation of 0.13.

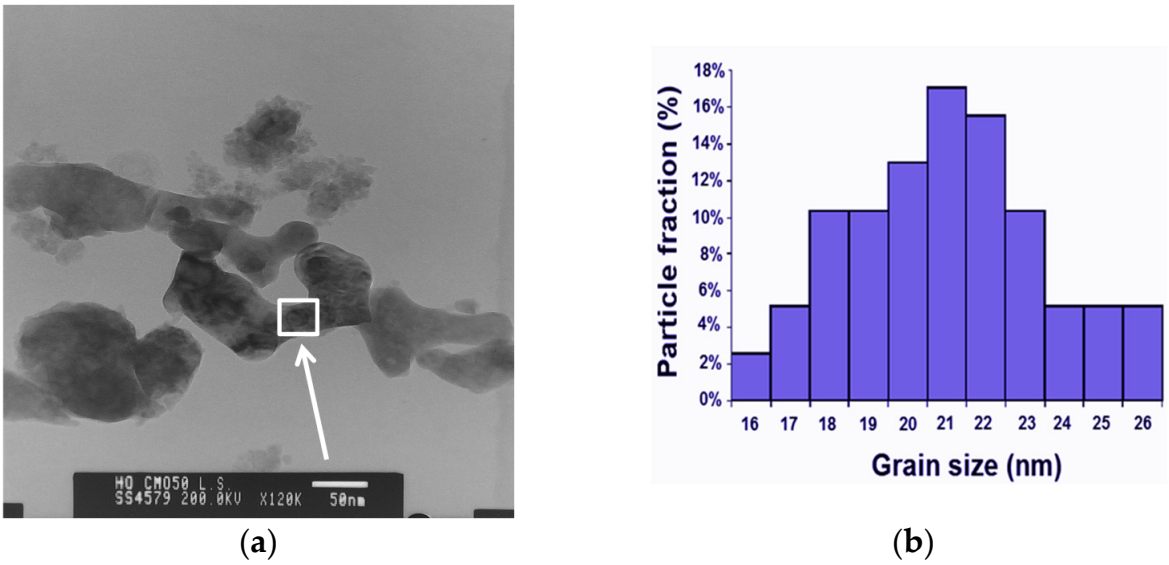

Figure 2. (**a**) High-resolution transmission electron microscopy image showing several agglomerates of nanoparticles. The white square indicated by the arrow highlights a single nanoparticle; (**b**) grain size distribution of the nanoparticles.

Figure 3 displays the neutron powder diffraction pattern collected at 300 K and refined by the Rietveld method, taking as the starting model the bulk *Pbnm* crystal structure [16]. At the best fitting, the refined nanocrystalline lattice parameters were a = 5.291(6) Å b = 5.435(6) Å, c = 7.472(6) Å, to be compared with the bulk values a = 5.3066(1) Å, b = 5.4686(1) Å, c = 7.4529(1) Å. With respect to the bulk, a and b are slightly contracted while c is elongated. Lattice parameters are in the relation $c/\sqrt{2} \cong a < b$. This means that at room temperature the orthorhombic distortion is mainly due to steric effects, i.e., to the small size of Ho/Ca species at A site, while the additional deformation due to the cooperative Jahn–Teller effect, which leads to the bulk O′ structure [32], is very weak. The diffractometric crystallite size was found to be 22 ± 4 nm, which, if compared to the particle size determined by high-resolution transmission electron microscopy, indicates that most particles are monocrystalline.

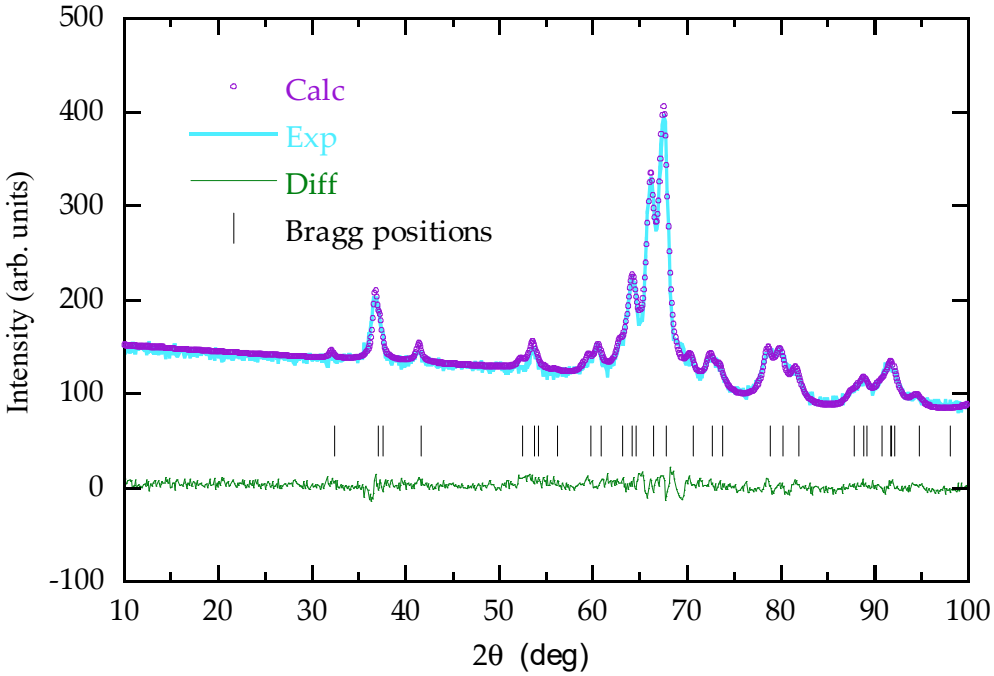

Figure 3. Rietveld refinement plot for the neutron powder diffraction pattern collected at 300 K. The cyan solid line in the upper field represents the observed intensity data, while the calculated pattern is superposed and drawn as purple empty dots. The small black vertical bars indicate the positions of the allowed Bragg reflections for the orthorhombic phase. The difference between the observed and calculated patterns is plotted in the lower field as a green solid line. Rietveld discrepancy values are R-profile R_p = 2.7 %, R-weighted profile R_{wp} = 3.4%, goodness-of-fit GoF (i.e., χ^2) = 1.3, R-Bragg R_B = 3.4%.

The orthorhombic unit cell is shown in Figure 4 with selected bond lengths and angles. At room temperature, the c axis elongation in $Ho_{0.5}Ca_{0.5}MnO_3$ nanoparticles is accommodated not via octahedra deformation but through the increase of the Mn-O_{ap}-Mn bond angle from the bulk value θ = 152.2° to θ = 158.1°. This is interesting, since for a double-exchange system, the width W_σ of the tight-binding band for itinerant Mn^{3+} 3d e_g electrons is strictly related to the bond bending angle (π − θ) as $W_\sigma = \varepsilon_\sigma \lambda_\sigma^2 \cos(\pi - \theta) \langle \cos(\Theta_{ij}/2) \rangle$, in which ε_σ is the one-electron energy, λ_σ is the overlap integral, and Θ_{ij} is the angle formed by the underlying localized Mn 3d t_{2g} (i.e., d(xy), d(xz), d(yz)) core spins [33]. With such an opened Mn-O_{ap}-Mn angle, the e_g electron, formally belonging to Mn^{3+}, might attain a certain degree of delocalization on Mn pairs along [001] [34], leading to the formation of manganese dimers coupled ferromagnetically by double exchange Zener polarons [35] and opening a FM channel within the electron-localized AFM bulk-like matrix. Indeed, the value of 158° is critical for the previous scenario to take place at the doping level x = 0.3 [36]. Other nanosize half-doped manganites, in which CO and antiferromagnetism are completely suppressed, have been reported to display even larger in-plane or out-of-plane bond angles [26].

The temperature variations of the refined orthorhombic cell parameters are shown in Figure 5a. All refinements were carried out in terms of a single *Pbnm* phase, i.e., without attempting at using the lower monoclinic symmetry required in presence of CO to distinguish Mn^{3+} and Mn^{4+} sites [16], given the absence of superlattice reflections related to CO and the low data resolution. It can be noted that, while c contracts non-linearly on cooling, the in-plane parameters a and b remain practically constant down to about 100 K, with only a modest initial reduction. This is different from what happens in bulk $Ho_{0.5}Ca_{0.5}MnO_3$, in which the arising of both OO and CO is evidenced by the typical, albeit much less pronounced, with respect to other CO half-doped systems, increase of both a and b on cooling in the range 300 K < T < 250 K, with a concomitant decrease of c [16].

Therefore, in $Ho_{0.5}Ca_{0.5}MnO_3$ nanoparticles, there is no clear structural evidence for charge ordering in terms of unit cell metrics. Below room temperature, the relations among a, b, and c become compatible with orbital ordering ($c/\sqrt{2} < a < b$), with increasing cooperative Jahn–Teller distortion on cooling.

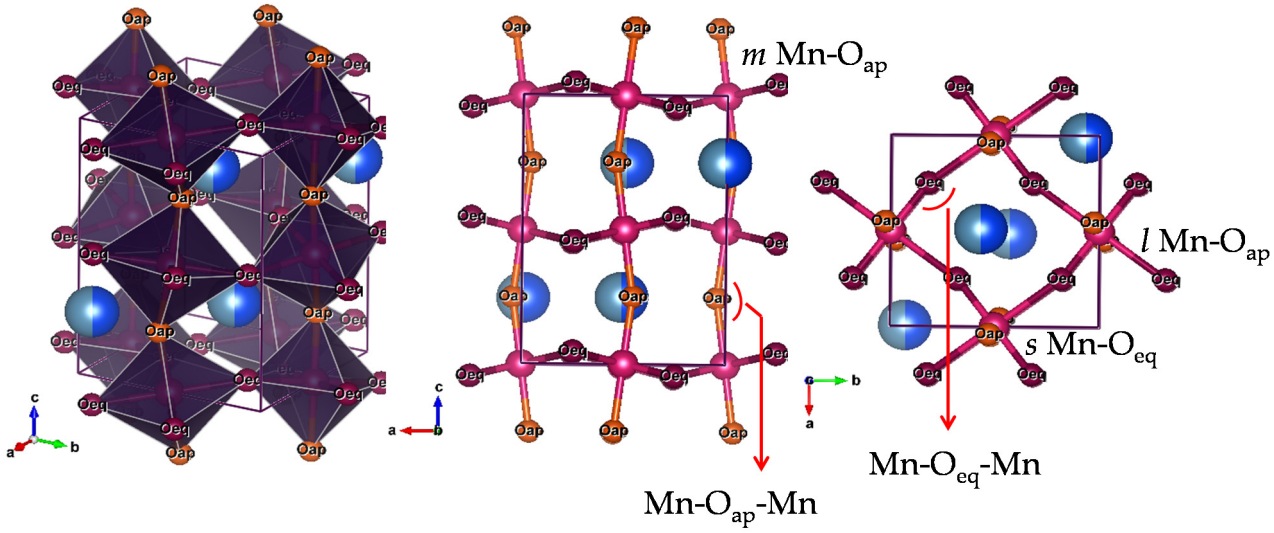

(**a**) (**b**) (**c**)

Figure 4. Room temperature orthorhombic *Pbnm* unit cell of $Ho_{0.5}Ca_{0.5}MnO_3$ nanoparticles. (**a**) Interconnection of MnO_3 octahedra through apical (O_{ap}) and equatorial (O_{eq}) oxygen atoms. Mn atoms are within the octahedra. The Ho/Ca sites are depicted as virtual balls composed of half Ho and half Ca of different blue shades. (**b**) Projection of the unit cell along the [010] orthorhombic direction. (**c**) Projection of the unit cell along the [001] orthorhombic direction. The mean values of the intermediate, short, and long Mn-O bond distances (respectively *m* Mn-O_{ap}, *s* Mn-O_{eq}, *l* Mn-O_{eq}) and of the Mn-O_{ap}-Mn and Mn-O_{eq}-Mn bond angles are: Mn-O_{eq}-Mn = 151.4°, Mn-O_{ap}-Mn = 158. 1°; *m* Mn-O_{ap} = 1.91 Å, *s* Mn-O_{eq} = 1.87 Å, *l* Mn-O_{eq} = 2.05 Å.

The c axis contraction on cooling is accommodated by increasing the distortion of the MnO_6 units, while the Mn-O_{ap}-Mn bond angle remains almost unaffected. The temperature evolution of such distortion can be evaluated in terms of the three (medium m, short s, long l) Mn-O bond distances. As shown in Figure 5b, the apical Mn-O_{ap} distance remains intermediate between the two equatorial Mn-O_{eq} ones in the analyzed temperature range, as expected for a Jahn–Teller distorted *Pbnm* phase with OO. The Jahn–Teller effect in *Pbnm* $RE_{0.5}Ca_{0.5}MnO_3$ phases is in fact dominated by the orthorhombic Q_2 active mode [37], which gives rise to alternating short and long s and l Mn-O distances in the (a,b) plane.

The contribution of the typical tetragonal mode Q_3, quantified by the deviation of the m length from the average (l + s)/2, is shown in Figure 5c. It can be seen that m < (l + s)/2 in the whole temperature range, indicating a Q_3 contribution with apical compression of the MnO_6 units ($Q_3 < 0$) along the dz^2-type orbital direction. The Q_3-type apical compression increases slightly on cooling. The major octahedra rearrangement takes place in the temperature range 100 K < T < 250 K. The previous results will be taken into account in the discussion of the magnetization measurements that will be presented in the following.

The ZFC-FC magnetization curves $M_{ZFC}(T)$ and $M_{FC}(T)$ of the nanoparticles, measured in H = 25 Oe, are shown in Figure 6a. The analogous curves for a micrometric sample prepared according to [16], representative of the bulk behavior, are also reported for comparison (Figure 6b).

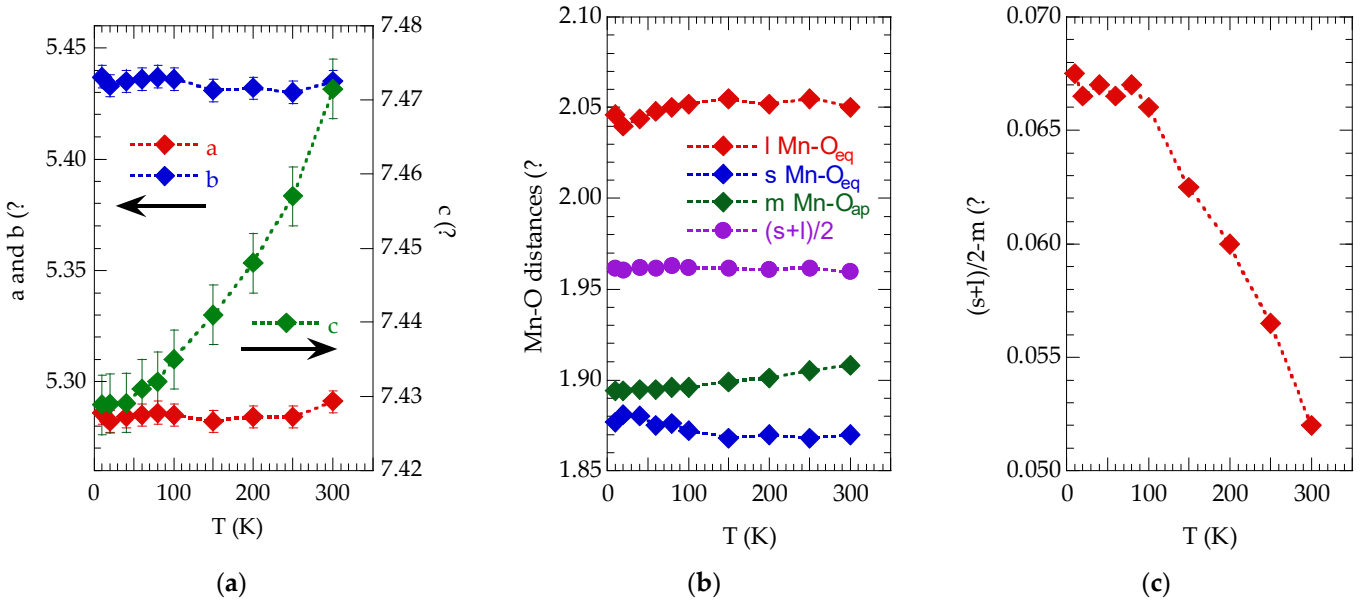

Figure 5. (**a**) Temperature dependence of the orthorhombic *Pbnm* lattice parameters. (**b**) Temperature dependence of the Mn-O distances and of the mean (s + l)/2 of the two equatorial short (s Mn-O_{eq}) and long (l Mn-O_{eq}) ones. (**c**) Temperature dependence of the Q_3-type apical octahedra compression (see text for details).

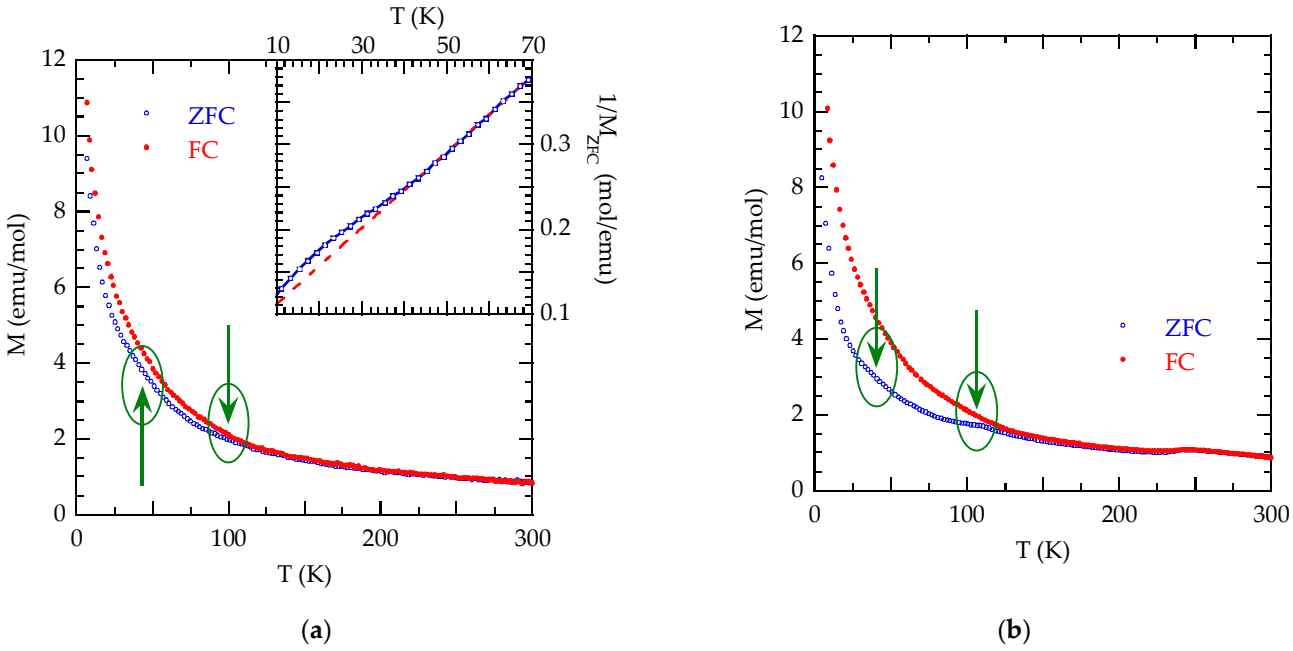

Figure 6. (**a**) Zero-field-cooled (ZFC, blue empty dots), field-cooled (FC, red full dots) magnetization curves of the nanometric sample recorded at H = 25 Oe. Green arrows and ellipses are guides for the eye for the identification of the transitions. Inset displays the inverse ZFC branch. The straight red line is a guide for the eye to evidence the deviation from the linear behavior on cooling. (**b**) Corresponding ZFC-FC magnetization curves for the micrometric sample.

In the bulk, CO manifests itself as a bump in M(T) dependence—both FC and ZFC—with $T_{CO} \approx 250$ K, which is absent in the nanoparticles. On cooling, both the micro and nanometric samples enter into a canted AFM phase. The bulk Néel point is easily identified at about 110 K, where the ZFC Curie-type magnetization has a clear inflection and the ZFC-FC irreversibility begins. In the absence of such ZFC anomaly, the Néel point of the

nanoparticles is tentatively set at about 105 K, corresponding to the onset of the ZFC-FC irreversibility. The lower transition at about 40 K, rather well marked in the ZFC branch of the bulk, is much less visible in the nanoparticles, but it appears in the plot of inverse ZFC magnetization as a function of temperature (Inset of Figure 6a) as a deviation from linear behavior. Overall, apart from the absence of a clear signature related to CO, the sequence of transitions at the nanometric length scale seems to be bulk-like. To go deeper into the analysis, we considered the temperature dependence of the FC magnetization of the nanoparticles at 25 Oe, after subtraction of the strong Ho^{3+} contribution (with its molar susceptibility χ defined as M/H and modeled as $\chi(T) = \frac{N_A}{2}\frac{(10.6)^2}{3k_B T}\mu_B^2$ ($N_A = 6.023 \times 10^{23}$ mol^{-1} Avogadro number, $k_B = 1.38 \times 10^{-16}$ eV/K Boltzmann constant, 10.6 theoretical effective magnetic moment of free Ho^{3+} expressed in Bohr magnetons $\mu_B = 9.274\ 10^{-21}$ emu). In this way, we intended to put under evidence the behavior of Mn ions (too heavily masked in nanoparticles) that are the only ones responsible for the CO phenomenon and the magnetic transitions. The details of the subtraction are shown in Figure 7a, in which we display the experimental FC M(T) curve at 25 Oe, the aforementioned contribution of paramagnetic Ho^{3+} and the Curie-type M(T) magnetization for the sum of paramagnetic Mn and Ho species, with effective magnetic moment calculated from the free ions values as $\left\{1/2\left[\mu_{eff}^2\left(Mn^{4+}\right) + \mu_{eff}^2\left(Mn^{3+}\right) + \mu_{eff}^2\left(Ho^{3+}\right)\right]\right\}^{1/2}$, in the absence of any magnetic transition. The development of AFM correlations and long-range ordering in the Mn sublattice produce an increasing difference between the experimental and calculated total curve on cooling below 140 K. However, even under the assumption that Mn ions do not contribute anymore to M(T) below their AFM transition, one can see that the Ho^{3+} contribution is overestimated on further cooling. This may indicate that the Ho^{3+} 4f electronic levels, split in the low symmetry crystal field, are affected by the exchange field of the ordered Mn sublattice, with a complex variation of the apparent Curie constant on cooling. Coupling among 4f and 3d electrons has been already discussed for other CMR $RE_{1-x}Ca_xMnO_3$ systems, in particular for $Pr_{1-x}Ca_xMnO_3$ at various doping levels [36,38]. Aware of the low-temperature issues, we display in Figure 7b the holmium subtraction limited to the temperature range of interest for the manganese transitions. It appears that the ordering of Mn moments starts around 110 K, with a steep rise of M(T), with a small discontinuity at about 80 K and a subsequent increase up to a maximum, which, however, could depend on the mentioned onset of Ho-Mn interaction.

The features of the paramagnetic region (T > 110 K) emerge instead in the inverse magnetization as a function of temperature shown in Inset of Figure 7b. A single Curie–Weiss law cannot fit the entire temperature region above T_N (indicatively above 120 K), clearly, a net upward of 1/M(T) occurs distinguishing between a high temperature (HT) and a low temperature (LT) region above and below this upward trend, respectively. Linear fits in the HT and LT regions show strong antiferromagnetic correlations (i.e., high negative Weiss temperature) developing on cooling below about 220 K. The obtained ratio between the Curie constants C_{LT}/C_{HT} of 2.23 largely exceeds the value of 1.62 expected for the formation, below T_{CO}, of Zener polarons, according to the "bond centered" description of CO given by Daoud Aladine et al. [38], alternative to the site-centered model of Goodenough [10]. Indeed, the two very different equatorial short and long Mn-O bond distances obtained from the structural analysis are a straightforward indicator by their own of two crystallographically well-differentiated valence states of manganese atoms, resulting in a OO/CO pattern matching rather the bulk-like CO solution [7].

Figure 8 displays the hysteresis cycles measured at 5 K for the nanometric and micrometric samples. The open M(H) loops confirm a switchable magnetization of a canted phase or the presence of a small ferromagnetic component related to surface effects, not unexpected in such small particles. The coercive field H_c is 60 Oe for bulk and 110 Oe for the nano-sample, larger at the nanoscale possibly due to surface anisotropy effect [39].

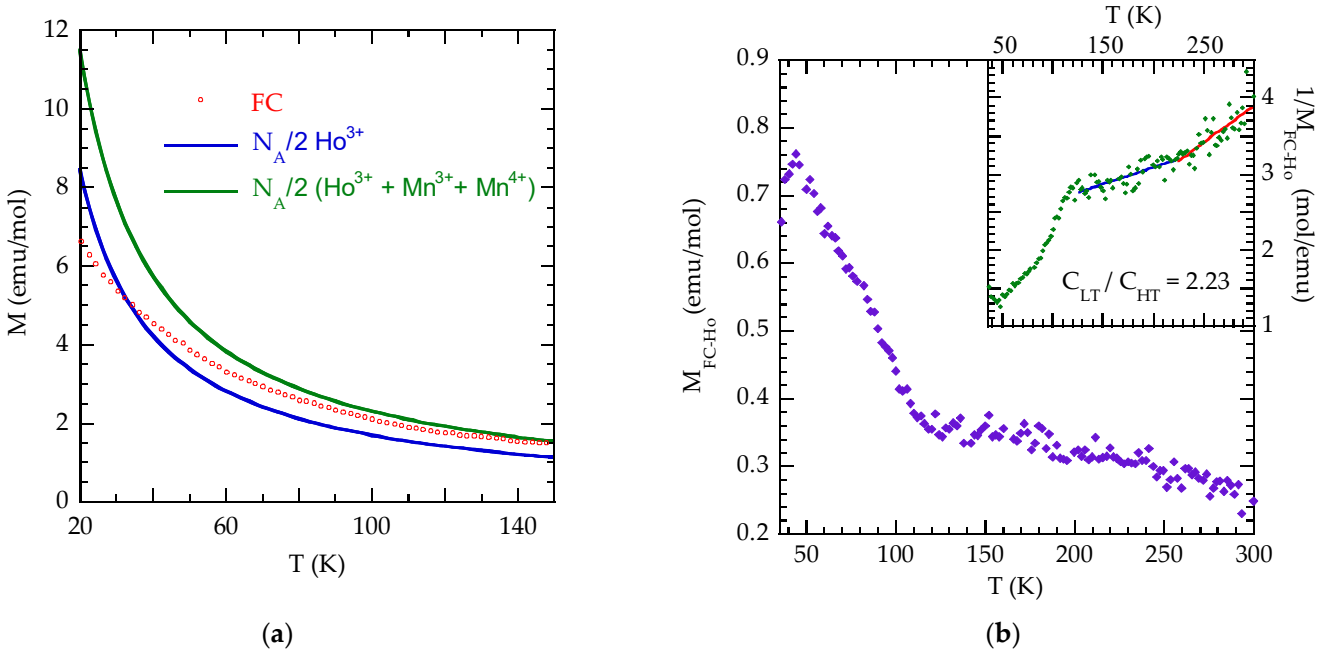

Figure 7. (**a**) Temperature dependence of the field-cooled magnetization recorded at H = 25 of $Ho_{0.5}Ca_{0.5}MnO_3$ nanoparticles (red points), calculated paramagnetic contribution of Ho^{3+} (blue continuous line) and total paramagnetic contribution of Ho plus Mn species (green continuous line), both treated as free ions (see text). (**b**) Temperature dependence of the field-cooled magnetization and of its inverse (shown in Inset) after subtraction of the strong Ho^{3+} paramagnetic contribution. The solid lines in Inset represent the linear fits in the high-temperature (HT) region (red) and in the low-temperature (LT) region (blue).

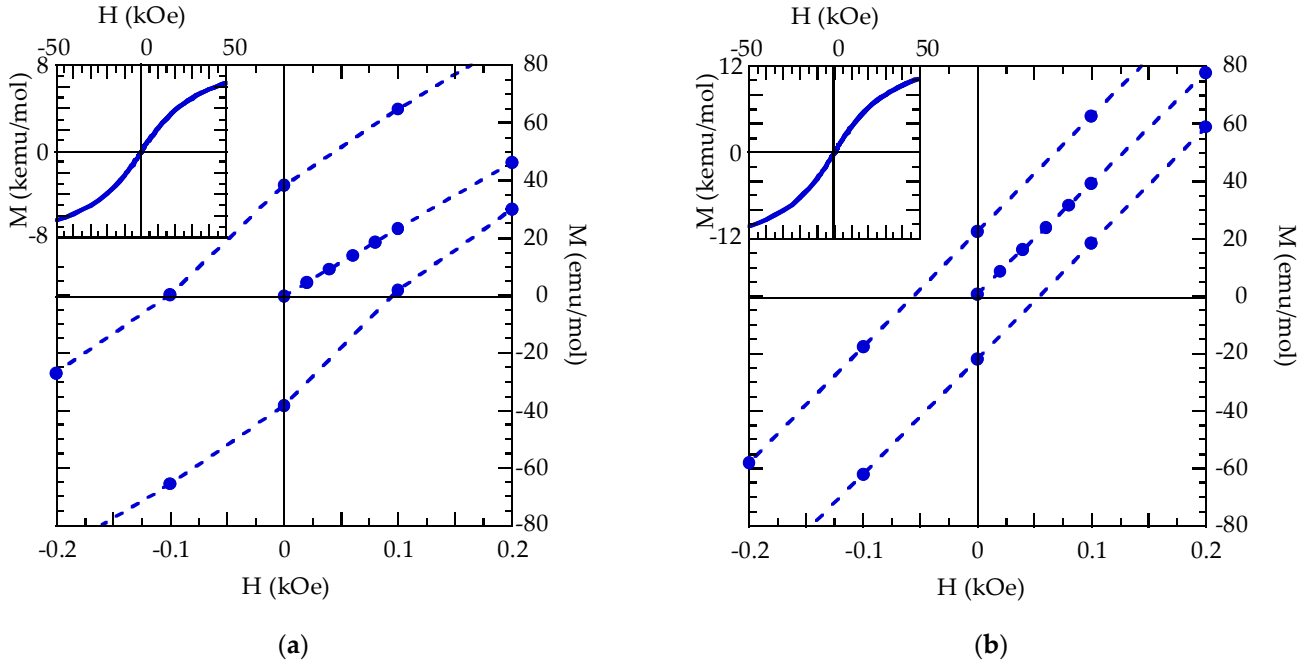

Figure 8. (**a**) Low magnetic field region of the hysteresis cycle of the nanometric sample measured at 5 K. (**b**) Low magnetic field region of the hysteresis cycle of the micrometric sample measured at 5 K. Insets show the complete hysteresis loops for the two samples.

In the light of the previous results, we now discuss the neutron diffraction experiments as it concerns the detection of magnetic reflections on cooling. Figure 9 shows the low

angle range of the diffraction pattern of the nanoparticles taken at different temperatures. Magnetic superlattice reflections arise below 100 K, indicating the transition towards the antiferromagnetic state. A first intense magnetic peak, at $2\theta = 25.9^{\circ}$, rises between 100 K and 80 K, while a second less intense one, at $2\theta = 18.6^{\circ}$, becomes visible at 60 K. Some considerations can be made with reference to the bulk CE-type AFM spin arrangement and its modified version called pseudo-CE-type. Both structures are formed by zigzag ferromagnetic chains in the (001) *Pbnm* plane, with in-plane antiferromagnetic inter-chain coupling, as discussed in Introduction (cfr Figure 1e). However, the stacking of the planar pattern along the [001] direction is antiferromagnetic in the CE-type structure, but ferromagnetic in the pseudo-CE-type one [40–42]. In both orderings, the result is a four-fold magnetic supercell 2a × 2b × c when referring to the *Pbnm* unit cell, with decoupled magnetic reflections for the Mn^{3+} and Mn^{4+} sublattices. Reflections coming from Mn^{3+} are indexed as (h/2 k l) with odd integer h, while those related to Mn^{4+} as (h/2 k/2 l) with odd integer h, k. Index l is an odd integer for CE-type and even integer for pseudo-CE-type. The two magnetic reflections shown in Figure 9 are indexed in the nuclear cell as CE-type ($\frac{1}{2}$ $\frac{1}{2}$ 1) (the one at higher 2θ angle) and pseudo-CE-type ($\frac{1}{2}$ $\frac{1}{2}$ 0) (the one at lower 2θ angle). The low-intensity bump that appears between them—the only one that refers to Mn^{3+} in this scheme—is indexed as a CE-type ($\frac{1}{2}$ 0 1). Figure 9 also shows the extent of long-range correlated AFM regions obtained by the Scherrer formula. Magnetic reflections with the l index of mixed parity have already been reported for charge ordered half-doped manganitesand explained, in most cases, in terms of strain driven phase-separation into two slightly different lattices (i.e., more or less compressed along c), associated to distinct OO/CO patterns, as in the case of $Pr_{0.5}Ca_{0.5}Mn_{0.97}Ga_{0.03}O_3$ [43] and $Pr_{0.5}Ca_{0.5}Mn_{1-x}Ti_xO_3$ [44]. This seems appealing for nanoparticles, since it immediately refers to a core-shell model, with the inner and outer parts of the particles undergoing distinct transitions. However, the bulk-like transition sequence suggests instead a single-phase scenario. In this context, we can mention the single-phase solution discussed for $Nd_{0.5}Ca_{0.5}MnO_{3.02}$ in presence of mixed l indexes [45], in which the in-plane components m_x and m_y of the magnetic moment in the (001) planes remain arranged according to a CE-type structure, while the component m_z in the [001] direction change to a pseudo-CE-type AFM order. Within the interval of confidence of the measurements, we show in Figure 10 the evolution of the Mn moment direction of $Ho_{0.5}Ca_{0.5}MnO_3$ nanoparticles, when diffraction data are treated as a single nuclear and magnetic phase. One may see that a gradual reorientation of the moment direction occurs between 80 and 20 K, with an increase of the out-of-plane m canting for both Mn^{3+} and Mn^{4+} crystallographic species with respect to the CE-type bulk structure.

Two final questions arise. The first one is whether the canted phase features glassy properties below 40 K, as proposed in [16] and discussed in detail for $Sm_{0.5}Ca_{0.5}MnO_3$ in [25]. We guess it does not, at least in the bulk. Indeed, Figure 11 shows the real part of the complex susceptibility of the micrometric $Ho_{0.5}Ca_{0.5}MnO_3$ sample, in which no frequency dependence can be detected in the whole temperature range. Attempts at analogous measurements for the nanopowders failed, owing to the high noise affecting the sample response. The second one is whether the presence of small amounts of secondary phases, which do not appear in diffraction analyses, might be responsible for the anomaly around 40 K in the low-field temperature-dependent magnetization (cfr inset of Figure 6a). Actually, 40 K is a temperature scale common to many magnetically ordered crystalline systems with Mn-O-Mn superexchange interactions, like hausmannite Mn_3O_4 (ferrimagnetic with T_N = 43 K) [46], perovskite-type Mn_2O_3 (T_N = 100 K and 49 K) [47], hexagonal, and orthorhombic $HoMnO_3$ themselves (spin reorientation at Tsr = 42 K and T_N = 40 K, respectively) [3–5]). The same temperature scale may well characterize doped manganite perovskites too. However, the question of magnetic secondary phases, raised for instance for $La_{0.7}Ce_{0.3}MnO_3$ and $La_{0.8}Hf_{0.2}MnO_3$ [48,49] and discussed in that case by reference to undetected MnO_2, should not be underestimated.

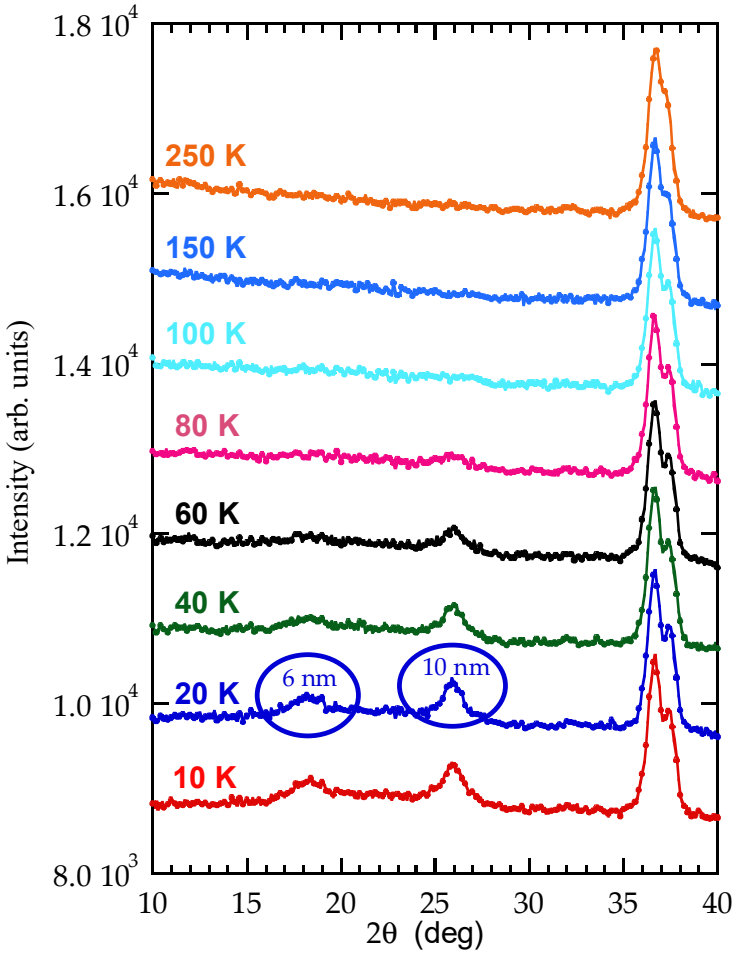

Figure 9. Low-angle scattering range of the neutron diffraction patterns of the $Ho_{0.5}Ca_{0.5}MnO_3$ nanoparticles taken at selected temperatures.

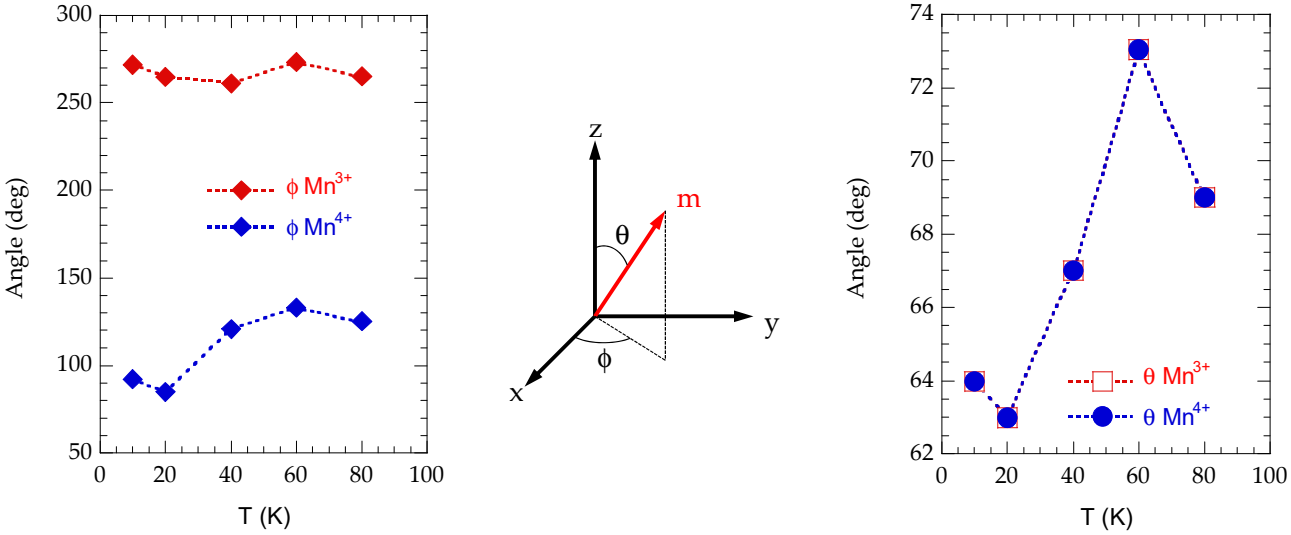

Figure 10. Spherical coordinates representation of the magnetic moment m of formally Mn^{3+} and Mn^{4+} ions, relative to the x-y-z axes of the *Pbnm* cell, as obtained by the neutron diffraction patterns of the nanoparticles refined with a single nuclear *Pbnm* phase and a single 2a × 2b × c magnetic supercell.

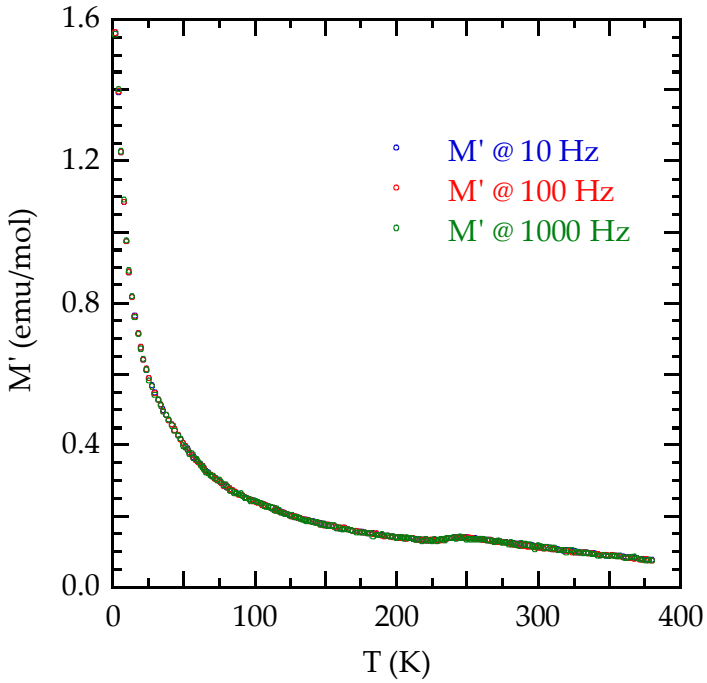

Figure 11. Real part of the AC magnetization as a function of temperature at three selected frequencies for the micrometric sample. Data were collected using a null DC magnetic field and an AC magnetic field H_{AC} = 3.5 Oe.

4. Conclusions

To summarize, we studied nanoparticles of the half-doped CMR manganites $Ho_{0.5}Ca_{0.5}MnO_3$, of about 20 nm in size, to investigate the role of reduced dimensions on the stability of the charge and orbital ordered CE-type antiferromagnetic structure characteristic of the bulk. We conclude that, contrary to what happens in most half-doped rare earth CMR manganites at this length scale, charge ordering and antiferromagnetism in $Ho_{0.5}Ca_{0.5}MnO_3$ are not suppressed. The proposed magnetic structure at the nanosize is based on a supercell metrically coincident with the bulk one, however, hosting a larger fraction of Zener double-exchange ferromagnetic interactions among Mn species. This result counts $Ho_{0.5}Ca_{0.5}MnO_3$ among those few half- or nearly half-doped CMR manganites, such as Sm_{1-x} Ca_xMnO_3 ($x \sim 0.5$) [50], in which the antiferromagnetic ground state is so robust that the Zener double exchange cannot emerge as a long-range interaction even by reducing the grain size to the nanoscale. An open issue remains concerning the nature of the transition seen around 40 K, which $Ho_{0.5}Ca_{0.5}MnO_3$ nanoparticles have in common with their bulk counterpart and with several other half-doped CMR phases. The question of whether such a transition is intrinsic—if it may be triggered by the rare-earth–manganese interaction, or if it is due to magnetic impurities—deserves further investigations.

Author Contributions: Conceptualization, A.G.L., F.C., M.F. and D.P.; methodology, A.G.L., F.C.; validation, A.G.L., F.C., G.M., M.F., D.P. and E.P.; formal analysis, A.G.L., F.C. and E.P.; investigation, A.G.L., F.C., E.P. and G.M.; resources, M.F., D.P. and G.M.; data curation, A.G.L., F.C. and E.P.; writing—original draft preparation, A.G.L., F.C.; writing—review and editing, A.G.L., G.M., M.F., E.P., D.P. and F.C.; visualization, A.G.L., F.C.; supervision, A.G.L.; project administration, A.G.L., M.F., D.P. and F.C.; funding acquisition, A.G.L. All authors have read and agreed to the published version of the manuscript.

Funding: G.M. acknowledges financial support from the PON AIM program (project AIM1809115—Activity No. 3—line 2.1).

Data Availability Statement: The data presented in this study are available upon request from the corresponding authors.

Acknowledgments: We thank Valentina Mameli for the X-ray fluorescence analysis and Luca Setti for his help in the synthesis and characterization of the samples.

Conflicts of Interest: The authors declare no conflict of interest.

References

1. Zener, C. Interaction between the d-shells in the transition metals. II. Ferromagnetic compounds of manganese with Perovskite structure. *Phys. Rev.* **1951**, *82*, 403–405. [CrossRef]
2. Anderson, P.W. New approach to the theory of superexchange interactions. *Career Theor. Phys. A* **2005**, *115*, 100–111. [CrossRef]
3. Vajk, O.P.; Kenzelmann, M.; Lynn, J.W.; Kim, S.B.; Cheong, S.W. Magnetic order and spin dynamics in ferroelectric $HoMnO_3$. *Phys. Rev. Lett.* **2005**, *94*, 087601. [CrossRef] [PubMed]
4. Lorenz, B.; Wang, Y.Q.; Sun, Y.Y.; Chu, C.W. Large magnetodielectric effects in orthorhombic $HoMnO_3$ and $YMnO_3$. *Phys. Rev. B Condens. Matter Mater. Phys.* **2004**, *70*, 212412. [CrossRef]
5. Lorenz, B.; Wang, Y.Q.; Chu, C.W. Ferroelectricity in perovskite $HoMnO_3$ and $YMnO_3$. *Phys. Rev. B Condens. Matter Mater. Phys.* **2007**, *76*, 104405. [CrossRef]
6. Rout, P.P.; Roul, B.K. Effect of Ca doping on enhancement of ferroelectricity and magnetism in $HoMnO_3$ multiferroic system. *J. Mater. Sci. Mater. Electron.* **2013**, *24*, 2493–2499. [CrossRef]
7. Goodenough, J.B. Theory of the role of covalence in the perovskite-type manganites [La,M(II)]MnO_3. *Phys. Rev.* **1955**, *100*, 564–573. [CrossRef]
8. Volja, D.; Yin, W.G.; Ku, W. Charge ordering in half-doped manganites: Weak charge disproportion and leading mechanisms. *EPL* **2010**, *89*, 27008. [CrossRef]
9. Barone, C.; Galdi, A.; Lampis, N.; Maritato, L.; Granozio, F.M.; Pagano, S.; Perna, P.; Radovic, M.; Scotti Di Uccio, U. Charge density waves enhance the electronic noise of manganites. *Phys. Rev. B Condens. Matter Mater. Phys.* **2009**, *80*, 115128. [CrossRef]
10. Nucara, A.; Maselli, P.; Calvani, P.; Sopracase, R.; Ortolani, M.; Gruener, G.; Guidi, M.C.; Schade, U.; García, J. Observation of charge-density-wave excitations in manganites. *Phys. Rev. Lett.* **2008**, *101*, 066407. [CrossRef] [PubMed]
11. Loudon, J.C.; Cox, S.; Williams, A.J.; Attfield, J.P.; Littlewood, P.B.; Midgley, P.A.; Mathur, N.D. Weak charge-lattice coupling requires reinterpretation of stripes of charge order in $La_{1-x}Ca_xMnO_3$. *Phys. Rev. Lett.* **2005**, *94*, 097202. [CrossRef] [PubMed]
12. Gershenson, M.E.; Podzorov, V.; Cheong, S.W.; Kiryukhin, V.; Kim, B.G. Martensitic accommodation strain and the metal-insulator transition in manganites. *Phys. Rev. B Condens. Matter Mater. Phys.* **2001**, *64*, 140406. [CrossRef]
13. Tokura, Y. Critical features of colossal magnetoresistive manganites. *Rep. Prog. Phys.* **2006**, *69*, 797–851. [CrossRef]
14. Jooss, C.; Wu, L.; Beetz, T.; Klie, R.F.; Beleggia, M.; Schofield, M.A.; Schramm, S.; Hoffmann, J.; Zhu, Y. Polaron melting and ordering as key mechanisms for colossal resistance effects in manganites. *Proc. Natl. Acad. Sci. USA* **2007**, *104*, 13597–13602. [CrossRef]
15. Kozlenko, D.P.; Jirák, Z.; Goncharenko, I.N.; Savenko, B.N. Suppression of the charge ordered state in $Pr_{0.75}Na_{0.25}MnO_3$ at high pressure. *J. Phys. Condens. Matter* **2004**, *16*, 5883–5895. [CrossRef]
16. Martinelli, A.; Ferretti, M.; Castellano, C.; Cimberle, M.R.; Masini, R.; Ritter, C. Neutron powder diffraction investigation on the crystal and magnetic structure of $(Ho_{0.50+x}Ca_{0.50-x})(Mn_{1-x}Cr_x)O_3$. *J. Phys. Condens. Matter* **2011**, *23*, 416005. [CrossRef]
17. López, J.; De Lima, O.F. Specific heat and magnetic properties of $Nd_{0.5}Sr_{0.5}MnO_3$ and $R_{0.5}Ca_{0.5}MnO_3$ (R = Nd, Sm, Dy, and Ho). *J. Appl. Phys.* **2003**, *94*, 4395–4399. [CrossRef]
18. Blasco, J.; García, J.; De Teresa, J.M.; Ibarra, M.R.; Pérez, J.; Algarabel, P.A.; Marquina, C.; Ritter, C. Charge ordering at room temperature in $Tb_{0.5}Ca_{0.5}MnO_3$. *J. Phys. Condens. Matter* **1997**, *9*, 10321–10331. [CrossRef]
19. Sarkar, T.; Raychaudhuri, A.K.; Chatterji, T. Size induced arrest of the room temperature crystallographic structure in nanoparticles of $La_{0.5}Ca_{0.5}MnO_3$. *Appl. Phys. Lett.* **2008**, *92*, 123104. [CrossRef]
20. Nagapriya, K.S.; Raychaudhuri, A.K.; Bansal, B.; Venkataraman, V.; Parashar, S.; Rao, C.N.R. Collapse of the charge-ordering state at high magnetic fields in the rare-earth manganite $Pr_{0.63}Ca_{0.37}MnO_3$. *Phys. Rev. B Condens. Matter Mater. Phys.* **2005**, *71*, 024426. [CrossRef]
21. Glezer, A.M.; Blinova, E.N.; Pozdnyakov, V.A.; Shelyakov, A.V. Martensite transformation in nanoparticles and nanomaterials. *J. Nanoparticle Res.* **2003**, *5*, 551–560. [CrossRef]
22. Balaev, D.A.; Krasikov, A.A.; Popkov, S.I.; Semenov, S.V.; Volochaev, M.N.; Velikanov, D.A.; Kirillov, V.L.; Martyanov, O.N. Uncompensated magnetic moment and surface and size effects in few-nanometer antiferromagnetic NiO particles. *J. Magn. Magn. Mater.* **2021**, *539*, 168343. [CrossRef]
23. Chatterji, T.; Su, Y.; Iles, G.N.; Lee, Y.C.; Khandhar, A.P.; Krishnan, K.M. Antiferromagnetic spin correlations in MnO nanoparticles. *J. Magn. Magn. Mater.* **2010**, *322*, 3333–3336. [CrossRef]
24. Wesselinowa, J.M. Size and anisotropy effects on magnetic properties of antiferromagnetic nanoparticles. *J. Magn. Magn. Mater.* **2010**, *322*, 234–237. [CrossRef]
25. Giri, S.K.; Poddar, A.; Nath, T.K. Surface spin glass and exchange bias effect in $Sm_{0.5}Ca_{0.5}MnO_3$ manganites nano particles. *AIP Adv.* **2011**, *1*, 032110. [CrossRef]
26. Shankar, U.; Singh, A.K. Origin of Suppression of Charge Ordering Transition in Nanocrystalline $Ln_{0.5}Ca_{0.5}MnO_3$ (Ln = La, Nd, Pr) Ceramics. *J. Phys. Chem. C* **2015**, *119*, 28620–28630. [CrossRef]

27. Pechini, M.P. Method of Preparing Lead and Alkalne Earth Titanates and Nibates and Coatting Method Using the Same to Form a Capacitor. U.S. Patent 3,330,697, 11 July 1967.
28. Martinelli, A.; Ferretti, M. The crystal structure of $(Ho_{0.50}Ca_{0.50})MnO_3$ and its evolution with Cr doping: A Rietveld refinement investigation. *Powder Diffr.* **2005**, *20*, 22–26. [CrossRef]
29. Rodríguez-Carvajal, J. FULLPROF: A program for Rietveld Refinement and Pattern Matching Analysis Abstracts of the Satellite Meeting on Powder Diffraction of the XV Congress of the IUCr, 127, Toulouse, France. 1990. Available online: https://www.bibsonomy.org/bibtex/1f3e4945ad804f38471c6ad3a513f1e76/jamasi (accessed on 5 December 2021).
30. Qureshi, N. Instrumental aspects. *EPJ Web Conf.* **2017**, *155*, 00002. [CrossRef]
31. Hansen, T.C.; Henry, P.F.; Fischer, H.E.; Torregrossa, J.; Convert, P. The D20 instrument at the ILL: A versatile high-intensity two-axis neutron diffractometer. *Meas. Sci. Technol.* **2008**, *19*, 034001. [CrossRef]
32. Jirák, Z.; Krupička, S.; Šimša, Z.; Dlouhá, M.; Vratislav, S. Neutron diffraction study of $Pr_{1-x}Ca_xMnO_3$ perovskites. *J. Magn. Magn. Mater.* **1985**, *53*, 153–166. [CrossRef]
33. Goodenough, J.B. Electronic structure of CMR manganites (invited). *J. Appl. Phys.* **1997**, *81*, 5330–5335. [CrossRef]
34. Rivadulla, F.; López-Quintela, M.A.; Mira, J.; Rivas, J. Jahn-Teller vibrational anisotropy determines the magnetic structure in orthomanganites. *Phys. Rev. B— Condens. Matter Mater. Phys.* **2001**, *64*, 052403. [CrossRef]
35. Zhou, J.; Goodenough, J. Zener versus de Gennes ferromagnetism. *Phys. Rev. B Condens. Matter Mater. Phys.* **2000**, *62*, 3834–3838. [CrossRef]
36. Geddo Lehmann, A.; Congiu, F.; Lampis, N.; Miletto Granozio, F.; Perna, P.; Radovic, M.; Scotti Di Uccio, U. Magnetic properties of pseudomorphic epitaxial films of $Pr_{0.7}Ca_{0.3}MnO_3$ under different biaxial tensile stresses. *Phys. Rev. B Condens. Matter Mater. Phys.* **2010**, *82*, 014415. [CrossRef]
37. Kanamori, J. Crystal Distortion in Magnetic Compounds. *J. Appl. Phys.* **1960**, *31*, 14s–23s. [CrossRef]
38. Daoud-Aladine, A.; Rodríguez-Carvajal, J.; Pinsard-Gaudart, L.; Fernández-Díaz, M.T.; Revcolevschi, A. Zener Polaron Ordering in Half-Doped Manganites. *Phys. Rev. Lett.* **2002**, *89*, 097205. [CrossRef]
39. Wesselinowa, J.M.; Apostolova, I. Size, anisotropy and doping effects on the coercive field of ferromagnetic nanoparticles. *J. Phys. Condens. Matter* **2007**, *19*, 406235. [CrossRef] [PubMed]
40. Radaelli, P.; Cox, D.; Marezio, M. Charge, orbital, and magnetic ordering ins. *Phys. Rev. B Condens. Matter Mater. Phys.* **1997**, *55*, 3015–3023. [CrossRef]
41. Wollan, E.O.; Koehler, W.C. Neutron diffraction study of the magnetic properties of the series of perovskite-type compounds [(1-x)La,xCa]MnO_3. *Phys. Rev.* **1955**, *100*, 545–563. [CrossRef]
42. García-Munoz, J.L.; Frontera, C.; Aranda, M.A.G.; Ritter, C.; Llobet, A.; Respaud, M.; Goiran, M.; Rakoto, H.; Masson, O.; Vanacken, J.; et al. Charge and orbital order in rare-earth and Bi manganites: A comparison. *J. Solid State Chem.* **2003**, *171*, 84–89. [CrossRef]
43. Yaicle, C.; Fauth, F.; Martin, C.; Retoux, R.; Jirak, Z.; Hervieu, M.; Raveau, B.; Maignan, A. $Pr_{0.}5Ca_{0.5}Mn_{0.97}Ga_{0.03}O_3$, a strongly strained system due to the coexistence of two orbital ordered phases at low temperature. *J. Solid State Chem.* **2005**, *178*, 1652–1660. [CrossRef]
44. Frontera, C.; Beran, P.; Bellido, N.; Hernández-Velasco, J.; García-Muñoz, J.L. Effects of d0 substitution on phase competition in $Pr_{0.50}Ca_{0.50}Mn_{1-x}TixO_3$. *J. Appl. Phys.* **2008**, *103*, 07F719. [CrossRef]
45. Frontera, C.; García-Muñoz, J.L.; Llobet, A. Dependence of the physical properties of on the oxidation state of Mn. *Phys. Rev. B Condens. Matter Mater. Phys.* **2000**, *62*, 3002–3005. [CrossRef]
46. Dwight, K.; Menyuk, N. Magnetic properties of Mn_3O_4 and the canted spin problem. *Phys. Rev.* **1960**, *119*, 1470–1479. [CrossRef]
47. Cong, J.; Zhai, K.; Chai, Y.; Shang, D.; Khalyavin, D.D.; Johnson, R.D.; Kozlenko, D.P.; Kichanov, S.E.; Abakumov, A.M.; Tsirlin, A.A.; et al. Spin-induced multiferroicity in the binary perovskite manganite Mn_2O_3. *Nat. Commun.* **2018**, *9*, 2996. [CrossRef] [PubMed]
48. Sergeenkov, S.; Cardoso, C.A.; Andreeta, M.R.B.; Hernandes, A.C.; Leite, E.R.; Araújo-Moreira, F.M. Growth and magnetic properties of bulk electron doped $La_{0.7}Ce_{0.3}MnO_3$ manganites. *Phys. Status Solidi Appl. Mater. Sci.* **2011**, *208*, 1704–1707. [CrossRef]
49. Guo, E.J.; Wang, L.; Wu, Z.P.; Wang, L.; Lu, H.B.; Jin, K.J.; Gao, J. Phase diagram and spin-glass phenomena in electron-doped $La_{1-x}Hf_xMnO_3$ ($0.05 \leq x \leq 0.3$) manganite oxides. *J. Appl. Phys.* **2011**, *110*, 113914. [CrossRef]
50. Dasgupta, P.; Das, K.; Pakhira, S.; Mazumdar, C.; Mukherjee, S.; Mukherjee, S.; Poddar, A. Role of the stability of charge ordering in exchange bias effect in doped manganites. *Sci. Rep.* **2017**, *7*, 3220. [CrossRef] [PubMed]